Spin-dynamics simulations of the *XY* vector Blume-Emery-Griffiths model in three dimensions

J. A. Plascak,[1,2] Shan-Ho Tsai,[2,3] and D. P. Landau[2]
[1]*Departamento de Física, Instituto de Ciências Exatas, Universidade Federal de Minas Gerais, Caixa Postal 702, 30123-970 Belo Horizonte, MG, Brazil*
[2]*Center for Simulational Physics, University of Georgia, Athens, Georgia 30602, USA*
[3]*Enterprise Information Technology Services, University of Georgia, Athens, Georgia 30602, USA*
(Received 21 February 2007; published 9 July 2007)

We present extensive Monte Carlo spin-dynamics simulations of the vector Blume-Emery-Griffiths model with three-dimensional spins on a simple cubic lattice and periodic boundary conditions. For a range of Hamiltonian parameters, this model reproduces the phase diagram topology of the one experimentally observed for bulk mixtures of ^{3}He-^{4}He. Highly efficient decomposition time integration algorithms have been used to obtain the evolution of the equations of motion from which we have computed the dynamic structure factor $S(\mathbf{q},\omega)$ close to critical and tricritical points. The dispersion relation and the corresponding dynamic exponents have been obtained in the critical and multicritical transitions. We find that the dynamic critical exponents for in-plane and out-of-plane fluctuations are the same at the tricritical point but are in fact different along the critical line.

DOI: 10.1103/PhysRevE.76.011105 PACS number(s): 64.60.Ht, 75.10.−b, 75.40.Mg

I. INTRODUCTION

Classical spin systems have been the subject of intense theoretical investigations because they play a key role in the understanding of phase transitions, critical and multicritical behavior, scaling, and the universality hypothesis [1–4]. Apart from the range of the interactions and the spatial dimensionality, it is known that the universality class of such systems also depends on the symmetry and on the number of components n of the order parameter. Ising ($n=1$) and Heisenberg ($n=3$) models have been originally proposed to describe magnetism in pure and diluted materials [5–8] and are widely studied and employed in both classical and quantum contexts. However, great attention has also been devoted to the *XY* ($n=2$) model due to the richness of its phase diagram and the character of its transition. In particular, the two-dimensional *XY* model [9,10] is of special interest in the field of statistical mechanics because of its intriguing and unusual phase transition. In addition, the *XY* system is also the simplest spin model which allows propagating modes (the discrete nature of the Ising spins does not allow such excitations, resulting in a relaxational dynamics and no spin waves).

Recently, the study of the *XY* model has been motivated not only by its applicability in describing real magnetic materials [11–14] but also by its relevance to other condensed matter systems, e.g., liquid crystals [15] and superconductors [16–18], among others. It has long been recognized that the *XY* model of magnetism is in the same universality class as liquid ^{4}He. For this reason, it is also suitable for the study of the superfluid phase transition [19]. In fact, transport properties of the model close to criticality are related to the thermal conductivity of superfluid ^{4}He, which can be measured experimentally [20,21].

Another interesting class of real systems is the ^{3}He-^{4}He mixtures, in which the ^{3}He atoms act as impurities, reducing the superfluid transition temperature and driving the system towards phase separation [22,23]. In 1971, Blume, Emery, and Griffiths (BEG) proposed a simple discrete Ising-like spin model which could mimic the basic features of the bulk properties of the phase diagram of mixtures of ^{3}He-^{4}He [24]. However, the so-called BEG model carries some unphysical properties, for instance, it does not consider the rotational symmetry of the superfluid order parameter (the wave function of superfluid helium). In spite of that, the mean field solution of the model could account for the experimental phase diagram, including the tricritical point, for some reasonable values of the model parameters. Later, Berker and Nelson [25], and independently Cardy and Scalapino [26], proposed a planar rotator model to describe the behavior of films of ^{3}He-^{4}He mixtures, known as the vector Blume-Emery-Griffiths (VBEG) model. The model has been investigated in two dimensions using the Migdal-Kadanoff recursion relations and no tricritical point was found for any values of the parameters. Maciolek *et al.* [27] have studied the planar rotator VBEG model in three dimensions by mean field approximation and Monte Carlo simulations, and they did find tricritical points. The model, however, has no intrinsic spin dynamics (in the planar rotator model the spins are two-dimensional) and it is not suitable for studying propagating modes below the critical temperature. More recently, Freire *et al.* [28] have considered the *XY* vector Blume-Emery-Griffiths (*XY*-VBEG) model in three dimensions using Monte Carlo simulations. The phase diagrams are similar to those obtained for the corresponding planar rotator model but, in this case, the system has true dynamics.

It is our aim here to study the *XY*-VBEG model in three dimensions by employing extensive Monte Carlo spin-dynamics simulations. It is noteworthy that there is no information available on the tricritical dynamics in this class of systems. The plan of the paper is as follows. The model and simulations are described in the next section. The static properties are discussed in Sec. III while the dynamic behavior close to the critical and tricritical points are presented in Sec. IV. Some concluding remarks are given in Sec. V.

II. MODEL AND SIMULATIONS

A. Model

The *XY* vector Blume-Emery-Griffiths (*XY*-VBEG) model is an *XY* model embedded in a lattice-gas system defined by the Hamiltonian

$$\mathcal{H} = -J\sum_{\langle i,j\rangle}(S_i^x S_j^x + S_i^y S_j^y) - A\sum_{\langle i,j\rangle}\mathbf{S}_i^2\mathbf{S}_j^2 + \Delta\sum_{i=1}^{N}\mathbf{S}_i^2, \qquad (1)$$

where the first two sums are over nearest-neighbor pairs of atoms $\langle i,j\rangle$ and the last one is over all N sites of a simple cubic lattice with linear size L. J is the bilinear and A is the biquadratic exchange interaction, while Δ is the anisotropy crystal field. We have analyzed herein only the ferromagnetic case ($J>0$) which, despite having the same static properties as the antiferromagnetic counterpart ($J<0$), exhibits quite different dynamics [29]. $\mathbf{S}_i$ represents a three-dimensional classical spin whose magnitude is $|\mathbf{S}_i|=0$ or $|\mathbf{S}_i|=1$. There are thus two kinds of particles in the system: magnetic ones with $|\mathbf{S}_i|=1$ and nonmagnetic ones with $|\mathbf{S}_i|=0$. Magnetic particles represent ^{4}He atoms and the spin orientation accounts for the internal superfluid degrees of freedom. Nonmagnetic particles represent ^{3}He atoms. The components of $\mathbf{S}_i$ are S_i^x, S_i^y, and S_i^z, but two ^{4}He neighbors interact only via x and y components, hence leaving room for a true dynamics for the spins (which does not occur in the plane rotator model of Ref. [27]). In this way, the first term in the Hamiltonian takes into account the superfluidity, through the long-range ordering of the xy spin components. The second and third terms arise from a phenomenological modeling of the interaction energy between pairs of helium particles of the same or different species, as well as with the crystal field and, because either $|\mathbf{S}_i|=0$ or $|\mathbf{S}_i|=1$, the competition of these terms allows for the presence of "impurities" and a phase separation. Because of the usefulness of such a pseudospin model in describing superfluid mixtures of ^{3}He-^{4}He, throughout this paper we will often use the magnetic nomenclature.

B. Monte Carlo simulations

In order to study the phase diagram of the model, and also to get a set of equilibrium configurations needed to provide initial conditions for the equations of motion for the spin dynamics, we have used a hybrid Monte Carlo algorithm consisting of: (i) lattice gas moves; (ii) spin-reorientation updates; combined with a nonergodic version of (iii) the Wolff algorithm; and (iv) over-relaxation updates. Each update method is performed in sweeps over the whole lattice and each method (ii), (iii), or (iv) is preceded by a lattice-gas sweep.

The lattice gas update attempts to insert a magnetic particle, with a randomly selected spin orientation, at a site where a nonmagnetic one is located, or to replace the magnetic particle present at a site by a nonmagnetic one. The acceptance probability is given by the local heat-bath rule

$$p(\Delta E) = \frac{1}{\exp(\Delta E/k_B T)+1}, \qquad (2)$$

where ΔE is the change in configurational energy, according to Eq. (1), of the proposed move, k_B is the Boltzmann constant, and T is the temperature of the system.

The single spin-reorientation update is done as in the standard Metropolis algorithm; however, the acceptance probability is also given by the local heat-bath rule from Eq. (2). In this case, as well as for the lattice-gas move, the new spin direction is randomly selected from the uniform distribution on the unit sphere. The Wolff update affects only the in-plane components of the spin particles having $|\mathbf{S}_i|=1$, leaving the z component unchanged in order to obey detailed balance. As the cluster update never changes the z component of any spin, the Wolff algorithm alone is nonergodic. Analogously, the over-relaxation method is performed with a rotation solely of the in-plane component of the spins, in order to keep the configurational energy fixed. Both the over-relaxation update and the Wolff one are nonergodic, but together with the spin-reorientation and the lattice-gas moves, the combined algorithm is ergodic.

The Monte Carlo update algorithms (ii)–(iv), each one preceded by the update (i), are all combined using a hybrid Monte Carlo method [30]. Note that this combination reduces the correlations between successive configurations quite efficiently over a wider range of temperatures around the critical and tricritical points in the simulations. As discussed in Ref. [28], after testing different mixtures of the three algorithms we found that the best sampling was one spin-reorientation sweep, one Wolff cluster update, and one over-relaxation sweep, which defines a hybrid Monte Carlo step (MCS). The random number generator used is the routine RAN2 [31].

C. Spin dynamic simulations

To obtain the spin dynamics one must first get the equations of motion for the Hamiltonian $\mathcal{H}$. The easiest way to do this is to consider the quantum time evolution of $\mathbf{S}_i$, through the Heisenberg equations of motion for spin operators, with their usual commutation relations and, in the end, taking the classical limit. It turns out that with the Hamiltonian in Eq. (1) the equations of motion are given by the standard relation

$$\frac{d\mathbf{S}_i}{dt} = -\mathbf{S}_i \times \frac{\partial\mathcal{H}}{\partial\mathbf{S}_i}, \qquad (3)$$

where we have set $\hbar=1$ and $\frac{\partial\mathcal{H}}{\partial\mathbf{S}_i}=\mathbf{H}_{eff}^t$ is viewed as a total effective field on site i. This can be written as

$$\mathbf{H}_{eff}^t = \mathbf{H}_{eff} + \left[2\Delta - 2A\sum_{k=nn(i)} S_k^2\right]\mathbf{S}_i, \qquad (4)$$

where

$$\mathbf{H}_{eff} = \frac{\partial\mathcal{H}_{xy}}{\partial\mathbf{S}_i} = -J\sum_{k=nn(i)}(S_k^x\mathbf{i} + S_k^y\mathbf{j}) \qquad (5)$$

is the effective field resulting from the xy interaction part of the Hamiltonian (1), i.e.,

$$\mathcal{H}_{xy} = -J\sum_{\langle i,j\rangle}(S_i^x S_j^x + S_i^y S_j^y). \quad (6)$$

Because the second term in Eq. (4) is parallel to the spin $\mathbf{S}_i$, the spin dynamics of the *XY*-VBEG model given by Eq. (3) reduces to the time evolution governed by the equations of motion

$$\frac{d\mathbf{S}_i}{dt} = -\mathbf{S}_i \times \mathbf{H}_{eff}. \quad (7)$$

The above equation means that the time evolution of the system is governed only by the in-plane exchange interaction component $\mathcal{H}_{xy}$ of the Hamiltonian. Thus from the dynamic point of view, the system is equivalent to a site-diluted *XY* model due to the presence of ^{3}He atoms represented by the nonmagnetic sites. Because the effective field has units of interaction parameter J, the time variable in the spin dynamics simulations is measured in units of J, i.e., tJ is a dimensionless variable.

According to the spin dynamics method, the coupled equations of motion given by Eq. (7) have to be integrated numerically for each initial spin configuration. In particular, the theory of the spin dynamics simulations, using different modern integration methods, has been recently reviewed in several articles [32–34]. It is then possible to decide which method is more suitable for a given Hamiltonian. In the present case, the equations of motion have been integrated by using the fourth-order predictor-corrector method and also decomposition methods based on the second- and fourth-order Suzuki-Trotter approaches [35,36]. All the results were compared for some values of the Hamiltonian parameters. The fourth-order Suzuki-Trotter procedure has been shown to be the most efficient for this system due to the fact that, although it is the most time-consuming per time step, the time steps δt can be chosen to be larger than those required for the second-order Suzuki-Trotter procedure, or other more standard methods such as predictor-corrector ones. This method guarantees energy and spin-length conservation within machine precision and conservation of the z component of the magnetization within numerical truncation errors of the method. That is, by choosing appropriately the value of δt we can get fluctuations in the z component of the magnetization that are orders of magnitude smaller than the statistical fluctuations.

The fourth-order Suzuki-Trotter algorithm has been used with time step $\delta t = 0.2/J$, which guarantees sufficient accuracy regarding the conservation of the z component of the magnetization. Smaller time step $\delta t = 0.1/J$ has also been tested and no significant difference has been noted up to the maximum time of the simulation. The corresponding equations of motions have been integrated to a final time of $1000/J$; however, in several lattices, a final time of $400/J$ is enough to get the dynamic structure factor within a good resolution. The thermal averages were taken over 1000 initial configurations and the error bars of the dynamic quantities correspond to one standard deviation.

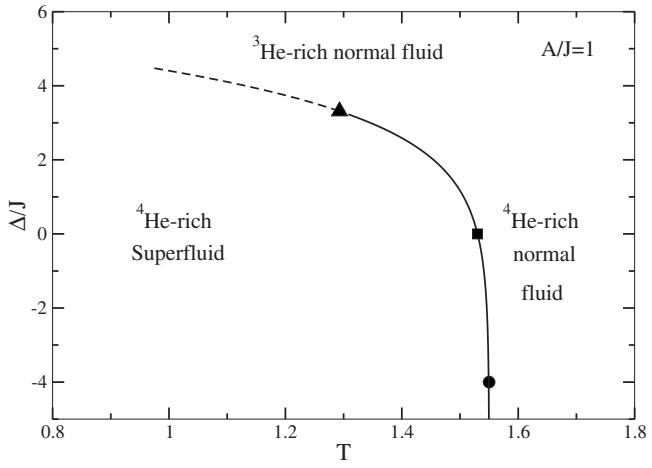

FIG. 1. Phase diagram of the *XY*-VBEG model defined in Eq. (1) for $J=1$ and $A=1$ in the $T-\Delta$ plane according to Ref. [28]. The full line represents a second-order phase transition between ^{4}He-rich superfluid and ^{4}He-rich normal fluid and the dashed line represents first-order phase transition between ^{4}He-rich superfluid and ^{3}He-rich normal fluid. The full triangle is the tricritical point. The full circle represents the limit where the system reduces to the pure *XY* model (i.e., all spins have $|\mathbf{S}_i|=1$) and the full square is the point at which we have done further simulations (the lines are a guide for the eyes).

III. RESULTS FOR STATIC PROPERTIES

The phase diagram of the model described by Eq. (1) has been determined in Ref. [28] for different values of the Hamiltonian parameters. The phase diagram in the temperature T (measured in units of J/k_B) versus crystal field Δ (measured in units of J) plane has a tricritical point for $A \leqslant 1$ (also measured in units of J). For larger values of A, e.g., $A=1.3$, the tricritical point decouples into a critical end point and a double critical end point (this decoupling should occur for some value of A between 1 and 1.3). In this work we will treat only the case $A=1$ whose phase diagram is schematically depicted in Fig. 1. Apart from the region close to the tricritical point, the first-order, as well as the second-order lines, have not been previously studied in detail in Ref. [28]. Although the full points in Fig. 1 do represent the actual temperatures in the thermodynamic limit for the model, the full line and the dashed line are just extrapolations. Regarding the first-order line we believe that it should go to $\Delta/J=6$ in the limit $T\to 0$, which has not been verified in Ref. [28] for larger lattices. For this reason, together with the fact that we need a set of initial configurations for the spin-dynamics simulation, we have employed the static hybrid Monte Carlo scheme described in the last section to determine the location of the critical temperature T_c, as well as the corresponding critical exponents at the second-order transition.

In the limit $\Delta\to-\infty$, the system reduces to the pure *XY* model, i.e., only magnetic particles are present on the lattice. This system has been treated by Krech and Landau [20] and the critical temperature has been located at $T_c=1.551\,83(12)$, with the critical exponents $\nu=0.6693(58)$, $\beta=0.3467(34)$, and $\gamma=1.315(12)$. This location is quite close

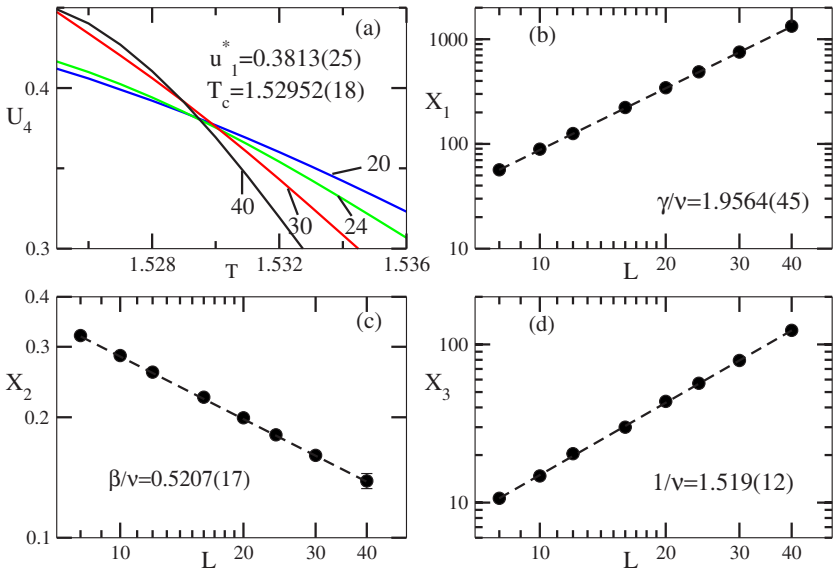

FIG. 2. (Color online) (a) Cumulant U_4 as a function of temperature for several lattice sizes. In (b)–(d) we have the log-log behavior of the size dependence of the quantities defined in Eq. (9) at T_c obtained from (a). The corresponding dashed lines are linear fits to the data. Where not indicated the error bars are smaller than the symbol sizes.

to the full circle in Fig. 1 for $\Delta=-4$. The results above are quite close to more recent estimates of Refs. [37,38].

We have additionally considered $\Delta=0.001$, which is the full square in Fig. 1 (this small value of the crystal field has been chosen for technical reasons: a value close to zero that could be simulated using the same code developed for any nonzero Δ). The critical temperature has been determined from the temperature and size dependence of the fourth-order Binder cumulant of the x component of the magnetization

$$U_4 = 1 - \frac{\langle M_x^4 \rangle}{3\langle M_x^2 \rangle^2}, \tag{8}$$

where $M_x^m = \left(\frac{1}{L^3}\Sigma_{i=1}^{L^3} S_i^x\right)^m$ and $m=2,4$ (the x component of the magnetization is given when $m=1$). We have chosen the above cumulant because it has been shown that it is more sensitive to temperature and size changes than the cumulant of the average square of the in-plane order parameter $\langle M_x^2 + M_y^2 \rangle$ [20].

The critical exponents have been estimated from the critical finite-size behavior of the mean value of the in-plane order parameter $\langle \sqrt{M_x^2+M_y^2} \rangle$, the average square of the in-plane order parameter $\langle M_x^2+M_y^2 \rangle$, and the temperature derivative of the latter, where $M_\alpha^m = \left(\frac{1}{L^3}\Sigma_{i=1}^{L^3} S_i^\alpha\right)^m$ with $\alpha=x$, y, or z. At $T=T_c$ one expects the following leading scaling behavior:

$$X_1 = L^3\langle M_x^2 + M_y^2 \rangle \sim L^{\gamma/\nu},$$

$$X_2 = \langle \sqrt{M_x^2 + M_y^2} \rangle \sim L^{-\beta/\nu},$$

$$X_3 = \frac{\partial}{\partial T} \ln\langle M_x^2 + M_y^2 \rangle \sim L^{1/\nu}, \tag{9}$$

where β, γ, and ν are the critical exponents of the order parameter, susceptibility, and correlation length, respectively.

For $\Delta=0.001$ we have employed the hybrid Monte Carlo algorithm for lattice sizes $L=8$, 10, 12, 16, 20, 24, 30, and 40 with periodic boundary conditions. After performing preliminary simulations to locate the crossings of the Binder cumulants, the single histogram reweighting technique has been implemented. In this case, the histograms have been taken with 10^6 MCS, after discarding the first 10^3 hybrid steps, for all lattice sizes. By analyzing the Monte Carlo time dependence it has been determined that the decay of the in-plane order parameter towards its equilibrium value took no more than 100 hybrid MCS, even for the largest lattice size. Figure 2 shows the results for the present thermodynamic quantities defined in Eqs. (8) and (9). The critical temperature has been located at $T_c=1.529\,52(18)$, which is smaller than, but still close to, the value at $\Delta\to-\infty$. It also turns out that corrections to scaling can be ignored within the statistical error of the quantities in Eq. (9). From the values of Figs. 2(b)–2(d) one gets $\nu=0.6583(52)$, $\beta=0.3428(30)$, and $\gamma=1.288(11)$, which are in quite good agreement with previous Monte Carlo estimates for a pure system [20]. From the above results, and also from the analysis done in Ref. [28] close to the tricritical point, where good finite-size scaling was obtained by using the exponents from Ref. [20] for the critical behavior, one sees that the second-order transition line in Fig. 1, regarding its static critical exponents, is a universal line. In addition, the algorithm to generate equilibrium configurations for the spin dynamics has been proven, in this way, to be indeed quite reliable.

IV. RESULTS FOR DYNAMIC STRUCTURE FACTOR

We have computed the dynamic structure factor $S^{\alpha\beta}(\mathbf{q},\omega)$, where α,β can be x,y, or z, $\mathbf{q}$ is the wave vector, ω is the frequency, and $S^{\alpha\beta}(\mathbf{q},\omega)$ is the time and space Fourier transform of the time-displaced and space-displaced spin-spin correlation function

$$\mathcal{S}^{\alpha\beta}(\mathbf{r}_i - \mathbf{r}_j, t-t') = \langle S_i^\alpha(t) S_j^\beta(t') \rangle - \langle S_i^\alpha(t) \rangle \langle S_j^\beta(t') \rangle. \tag{10}$$

In the above expression $\mathbf{r}_i$ and $\mathbf{r}_j$ are lattice vectors, and the spin components are computed at times t and t', respectively, evolved according to the equations of motion (7). The average $\langle \cdots \rangle$ is taken not only over the set of initial configura-

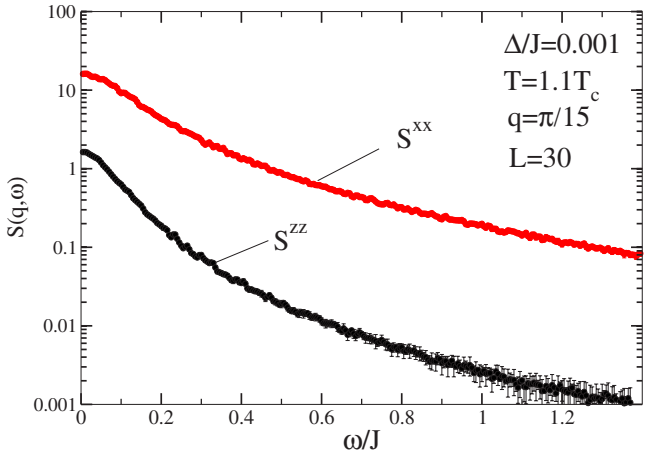

FIG. 3. (Color online) In-plane S^{xx} and out-of-plane S^{zz} components of the dynamic structure factor in the (100) direction for $T=1.1T_c$, $q=\pi/15$, and lattice size $L=30$ as a function of the dimensionless frequency ω/J.

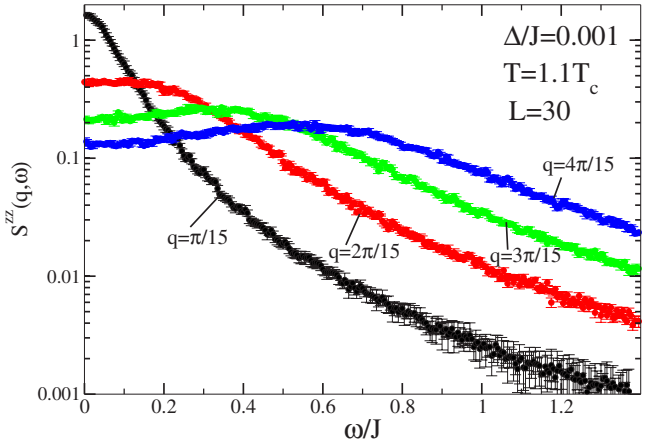

FIG. 4. (Color online) Out-of-plane S^{zz} component of the dynamic structure factor in the (100) direction for $T=1.1T_c$, $L=30$ as a function of the dimensionless frequency ω/J and $q=n_q\pi/15$ for $n_q=1,2,3,4$.

tions but also within the lattice for different space vectors $\mathbf{r}_i-\mathbf{r}_j$ and with different times t and t'.

The initial equilibrium configurations have been generated with the hybrid algorithm described in Sec. II. We have used simple cubic lattices with linear sizes $L=10$, 20, 24, 30, 40, 50, 60, and 80 with periodic boundary conditions. In what follows we discuss the behavior of the structure factor above, below, and at the critical and tricritical point. As in the static regime, all energetic quantities are measured in units of J and we have considered the phase diagram of Fig. 1 for $A=1$. In this case ω/J is a dimensionless quantity. The presentation is limited to $S^{\alpha\alpha}(\mathbf{q},\omega)$ for the wave vector $\mathbf{q}$ in the (100) direction since other lattice directions provide essentially the same information. We will also only present the in-plane xx component and the out-of-plane component zz. The in-plane component which we simply denote by xx is actually an average over S^{xx} and S^{yy} components, and the (100) direction is averaged over (100), (010), and (001) equivalent directions of the lattice.

A. Path through the critical line

The critical dynamics of the pure XY model on a simple cubic lattice, which can be measured at the full circle in Fig. 1, has been studied in detail in Ref. [20] by employing Monte Carlo spin-dynamics simulations. In the present case, the critical dynamics has been analyzed for $\Delta=0.001$, which corresponds to the full square in Fig. 1 and whose critical temperature was determined to be $T_c=1.529\,52$ (see Sec. III). The interest here is to check if the critical dynamics for the diluted XY model is also in the same universality class as its pure counterpart.

1. Dynamic structure factor in the paramagnetic regime

In the following we have chosen $T=1.1T_c$ where effects of criticality and finite-size scaling are almost absent. For this reason we could limit our spin dynamics simulations to smaller lattices and the results are presented for $L=30$. Figure 3 shows $S^{xx}(\mathbf{q},\omega)$ and $S^{zz}(\mathbf{q},\omega)$ for $\mathbf{q}=(q,0,0)$ at $q=\pi/15$ as a function of the dimensionless frequency ω/J. Both components show only a central peak for small q. Figure 4 depicts $S^{zz}(\mathbf{q},\omega)$ for the first four momenta $q=n_q\pi/15$ with $n_q=1,2,3,4$. For $n_q\geqslant 2$ we clearly see the presence of a broad maximum that moves to higher frequencies as q increases. The appearance of a spin-wave signature in this component above the critical temperature is visible from Fig. 4 and has been obtained in the pure XY model as well [20]. On the other hand, the frequency dependence of the in-plane $S^{xx}(\mathbf{q},\omega)$ is dominated only by a central peak for all q. This is illustrated in Fig. 5 for larger q near the Brillouin zone edge $q=\pi$. Note that S^{zz} is much smaller than S^{xx} for small values of q, as can be seen in Fig. 3, and becomes comparable to S^{xx} for large q (see Fig. 5).

2. Dynamic structure factor in the ordered regime

Again, to avoid critical finite-size effects below T_c we have chosen $T=0.9T_c$. At this temperature relatively small lattices are sufficient for obtaining the general behavior of the system. We have thus considered $L=30$, although smaller lattices yield the same results at our resolution. In this case the dynamics is dominated by spin waves. This is clear from

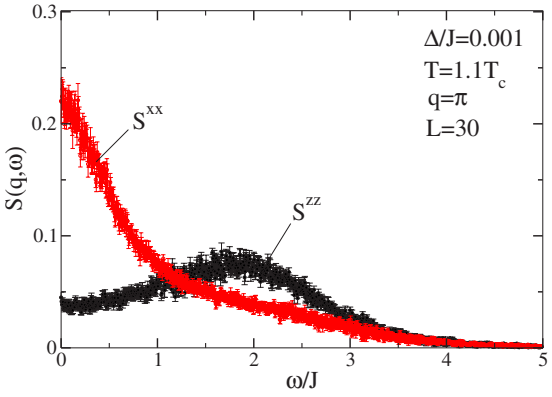

FIG. 5. (Color online) The same as Fig. 3 for $q=\pi$.

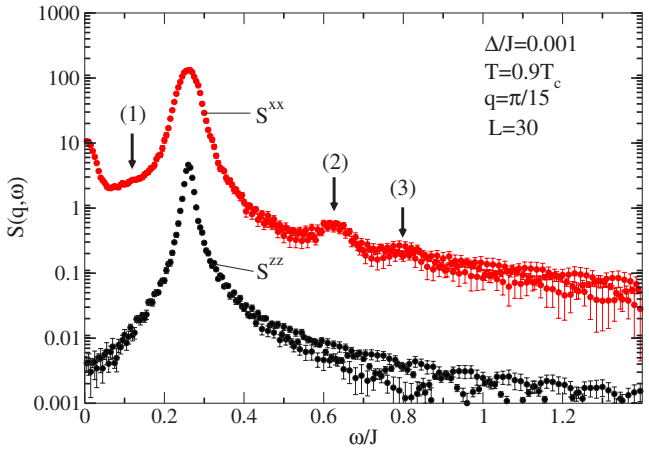

FIG. 6. (Color online) The same as Fig. 3 for $T=0.9T_c$. Apart from the dominant spin-wave peaks additional resonances (two-spin waves), indicated by the arrows, appear in the in-plane S^{xx} component at low intensities.

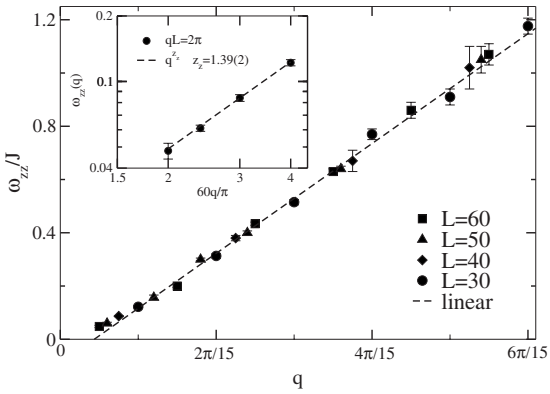

FIG. 8. Dispersion relation $\omega_{zz}(q)$ at $T=T_c$ and $\Delta=0.001$ for several lattice sizes. The dashed line is a linear fit to the data for $q<\pi/2$ in the (100) direction taking only the data for $L=30$. The inset shows a log-log plot of the dispersion relation $\omega_{zz}(q)$ for small values of the reduced wave vector in the (100) direction at $T=T_c$ and lattice sizes $L=30$, 40, 50, and 60. The dashed line is a linear fit to the data.

the behavior of $S(\mathbf{q},\omega)$ which is shown in Fig. 6 for $q=\pi/15$ in the (100) direction. The intensity of S^{xx} is around two orders of magnitude larger than S^{zz}, even at the peak intensity, which occurs at the same frequency. However, as in the pure model [20], there is fine structure in S^{xx} with lower intensities which are marked by the arrows in Fig. 6. As in Ref. [20], these resonances can be interpreted as two-spin-wave peaks and the arrows show the positions predicted from the spin-wave dispersion curve.

We have also measured the q dependence of the spin wave frequency $\omega(q)$ by just looking at the frequency of the maximum peak. The dispersion relation obtained for the (100) direction is depicted in Fig. 7. The functional form of the dispersion relation can be captured by a Fourier series transform of the type

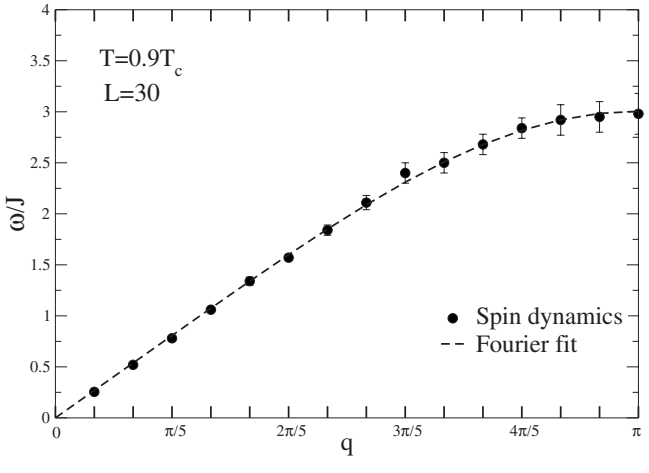

FIG. 7. Dispersion relation $\omega_{zz}(q)$ at $T=0.9T_c$ and $L=30$ in the (100) direction. The dashed line is a fit to the Fourier series of Eq. (11) with the first two terms. When not shown the error bars are smaller than the symbol sizes.

$$\omega(q)/J = a_1 \sin(q/2) + a_2 \sin(3q/2) + a_3 \sin(5q/2) + \cdots, \tag{11}$$

where the Fourier coefficients a_i are rapidly decreasing as i increases. By truncating after the second term in Eq. (11) one gets the least-squares fit shown in Fig. 7 with $a_1=2.986$ and $a_2=-0.109$.

3. Dynamic structure factor at T_c

At the critical temperature, the critical dynamics and the corresponding scaling behavior require much more numerical effort. We have thus considered lattice sizes $L=10$, 20, 24, 30, 40, 50, and 60, which are the same sizes employed in Ref. [20], in order to reach the scaling regime. We have measured the dispersion relations $\omega_{zz}(q)$ and $\omega_{xx}(q)$ from which estimates of the dynamic exponents z_z and z_x can be obtained. Figure 8 shows the dispersion relation $\omega_{zz}(q)$ at $T=T_c$ for several lattice sizes in the (100) direction. One can clearly see from the linear fit, taken with only the data for $L=30$ and for $q<\pi/2$, that deviations from the linearity become apparent for small values of q (which is different from the behavior shown in Fig. 7 for the ordered regime). The systematic deviation from the linearity seen for the larger lattices $L=40$, 50, and 60 is due to the critical effects that set in.

In particular, from the finite-size-scaling assumption one expects, at T_c and for sufficiently small q, the scaling relation to hold,

$$\omega_{\alpha\alpha} = q^{z_\alpha} \Omega_\alpha(qL), \tag{12}$$

where $\alpha=x,y$, or z, z_α are the corresponding dynamic exponents, and $\Omega_\alpha(qL)$ is a constant for a fixed value of qL or, equivalently, n_q. Since some systematic deviations occur for the smaller systems, we have considered the larger system sizes $L=30$, 40, 50, and 60. The inset in Fig. 8 shows a log-log plot of the dispersion relation $\omega_{zz}(q)$ for small values of q ($n_q=1$). A linear fit to the data gives $z_z=1.39(2)$, which

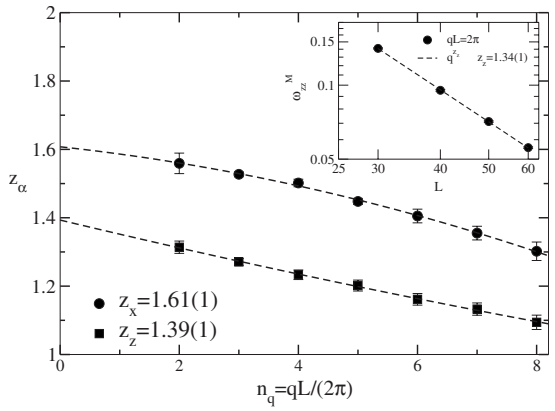

FIG. 9. Critical exponent z_α, $\alpha=z$ and x, as a function of n_q by using lattice sizes $L=30$, 40, 50, 60, and 80. The dashed lines are quadratic fits to the data. The inset shows a log-log plot of the median frequency ω_{zz}^M as a function of system size ($L=30$, 40, 50, and 60) for $n_q=1$ with the corresponding linear fit (dashed line) giving the critical exponent z_z.

is also substantially different from the mode-coupling prediction $z_z=1.5$ [39] and is comparable to the value $z_z=1.43(14)$ obtained in Ref. [20] for the pure model.

We have also done an independent and alternative estimate of the dynamic exponent provided by the median frequency $\omega_{\alpha\alpha}^M$ which is defined by the relation

$$\int_0^{\omega_{\alpha\alpha}^M} S^{\alpha\alpha}(\mathbf{q},\omega)d\omega = \frac{1}{2}G^{\alpha\alpha}(\mathbf{q}), \tag{13}$$

where $G^{\alpha\alpha}(\mathbf{q})$ is the static structure factor. The inset in Fig. 9 shows a log-log plot of the finite-size scaling behavior of the median frequency ω_{zz}^M which is expected to scale as

$$\omega_{\alpha\alpha}^M = L^{-z_\alpha} M_{\alpha\alpha}(qL) \tag{14}$$

at the critical point for $\alpha=z$. In this case we obtain $z_z=1.34(1)$ for $n_q=1$, which not only is in quite good agreement to that given by the dispersion relation in Fig. 8 but also is quite close to that obtained for the pure model using this very same quantity for $L\geqslant 30$ [20].

4. General remarks

The general behavior of the structure factor, as well as the dispersion relation, depicted in Figs. 3–9, are quite similar to those obtained previously for the pure three-dimensional *XY* model [20]. This is not surprising if we look at the ^{3}He concentration per site x_3 for $\Delta=0.001$: at $T=1.1T_c$ we have $x_3=0.025(2)$; at $T=T_c$ we have $x_3=0.014(1)$; and at $T=0.9T_c$ the concentration is $x_3=0.0054(1)$. For this value of Δ the presence of nonmagnetic ^{3}He atoms is still rather low so the thermodynamic properties of the diluted system are still close to its pure version. For instance, the critical temperature just drops from $T_c=1.551\,83(12)$ in the limit $\Delta\to-\infty$ to $T_c=1.529\,52(18)$ for $\Delta=0.001$, resulting in a critical slope for the diluted transition line

$$\frac{1}{T_c(x_3=0)}\left.\frac{dT}{dx_3}\right|_{x_3=0} = 1.027(2). \tag{15}$$

In this case, not only are the static exponents the same, but also the dynamic exponents remain the same as in the pure model. Thus the present dilution does not change the (static and dynamic) universality class of the *XY*-VBEG along the second-order transition line.

So far all that has been done was to compare the results from the pure system inclusive by using the same lattice sizes as before [20]. In order to go one step further, we have considered a larger lattice size than in the previous simulations ($L=80$) to better probe the asymptotic critical region in momentum. We have also used a more suitable approach to determine z_α by employing the finite-size scaling of $\omega_{\alpha\alpha}^M$ with several values of n_q and then extrapolating to $n_q=0$. We determined z_α for different values of n_q and the results are shown in Fig. 9. From a fit to a quadratic function of the type $z_\alpha+an_q+bn_q^2$, where z_α, a, and b are fitting parameters, one gets $z_z=1.39(1)$ and $z_x=1.61(1)$. We have not considered the data for $n_q=1$ because in this case the corresponding dynamic exponent, mainly for the in-plane component, does not follow the expected asymptotic regime shown in Fig. 9 [although they present a fair finite-size behavior as shown in the inset of Fig. 9; for instance, by including the extra data for $L=80$ in the inset of Fig. 9 one gets $z_z=1.35(1)$]. The extrapolated values from Fig. 9 clearly indicate that the in-plane and the out-of-plane dynamic critical exponents are indeed different (but still obeying the scaling relation $z_z+z_x=3$), in contrast to the antiferromagnetic isotropic Heisenberg model where a better statistic has shown that for sufficiently small q the dynamic critical exponent in fact agrees with the prediction by renormalization group theory $z_z=1.5$ [29].

B. Path through the tricritical point

We now turn our attention to the region close to the tricritical point. In this case we have from Ref. [28]

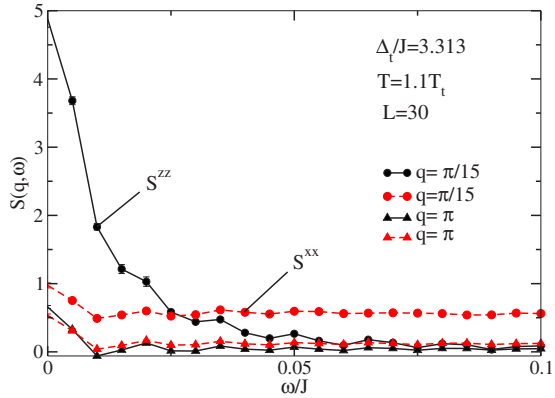

FIG. 10. (Color online) In-plane S^{xx} and out-of-plane S^{zz} components of the dynamic structure factor in the (100) direction for $T=1.1T_t$, $q=\pi/15$, and $q=\pi$, for the lattice size $L=30$ as a function of the dimensionless frequency ω/J.

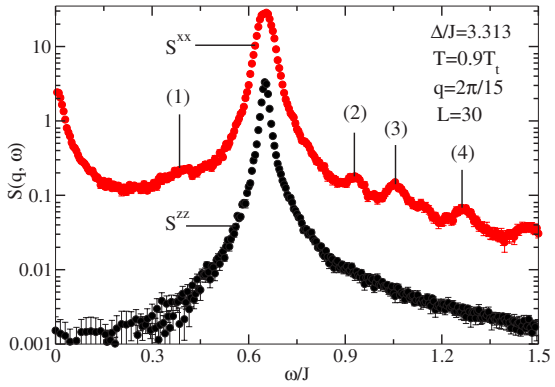

FIG. 11. (Color online) In-plane S^{xx} and out-of-plane S^{zz} components of the dynamic structure factor in the (100) direction for $T=0.9T_t$, $q=2\pi/15$ for the lattice size $L=30$ as a function of the dimensionless frequency ω/J. The arrows indicate the two-spin-wave peaks.

$\Delta_t=3.313(4)$ and $T_t=1.293(1)$. Thus as before, we will fix $\Delta=\Delta_t$ and change the temperature across the tricritical point.

1. Dynamic structure factor in the paramagnetic regime

In order to study the system where long-range effects can be neglected, we again chose $T=1.1T_t$. Figure 10 shows $S^{xx}(\mathbf{q},\omega)$ and $S^{zz}(\mathbf{q},\omega)$ for $\mathbf{q}=(q,0,0)$ for the smallest wave vector $q=\pi/15$, and also at the boundary of the Brillouin zone $q=\pi$, as a function of the dimensionless frequency ω/J. One can see that the decay is much faster than for smaller values of Δ (compare the range of the frequency axis in Figs. 10 and 3) and in this case we have only a central peak in both S^{zz} and S^{xx}, with no spin waves above T_t. In addition, in this case S^{xx} is smaller (but within the same order of magnitude) than S^{zz} for small q, and they are almost equal close to the Brillouin zone edge. This brusque change in the behavior of the structure factor can be understood due to the fact that now the system is in the normal fluid region rich in ^{3}He atoms (see Fig. 1). In fact, at this temperature we have $x_3=0.61(1)$, there being more nonmagnetic atoms than magnetic ones. So, in the normal fluid phase depicted in Fig. 1

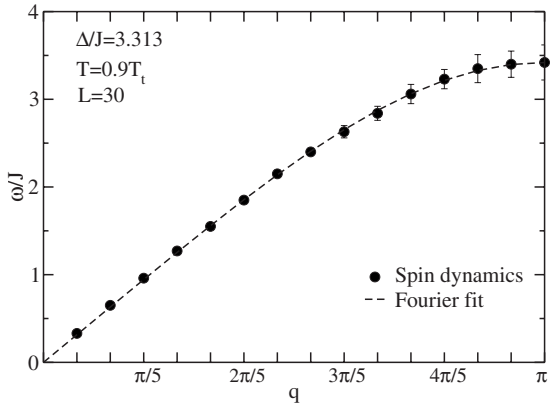

FIG. 12. Dispersion relation $\omega_{zz}(q)$ at $T=0.9T_t$ and $L=30$ in the (100) direction. The dashed line is a fit to the Fourier series of Eq. (11) with the first two terms.

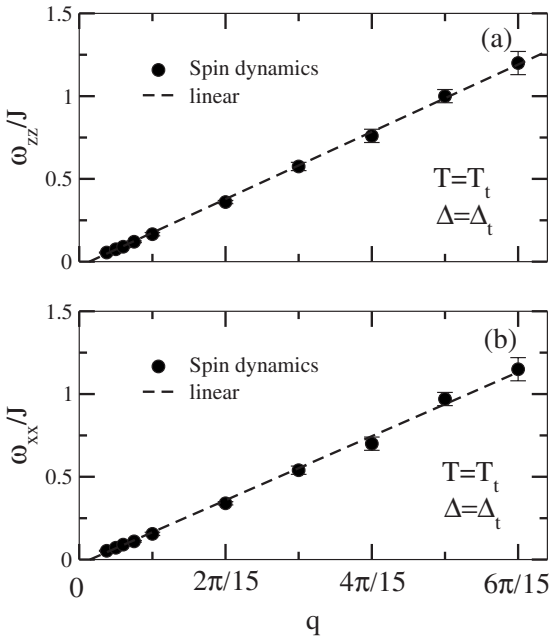

FIG. 13. Dispersion relation (a) $\omega_{zz}(q)$ and (b) $\omega_{xx}(q)$ at the tricritical point in the (100) direction. Dashed lines are linear fits to the data.

we can distinguish different dynamic behavior depending on whether the system is in the ^{4}He or ^{3}He rich phase.

2. Dynamic structure factor in the ordered regime

Figure 11 depicts the structure factor at $T=0.9T_t$. The in-plane S^{xx} and out-of-plane S^{zz} components of the dynamic structure factor in the (100) direction for $q=2\pi/15$ and the lattice size $L=30$ as a function of the dimensionless frequency ω/J are shown. Despite the intensity of S^{xx} being

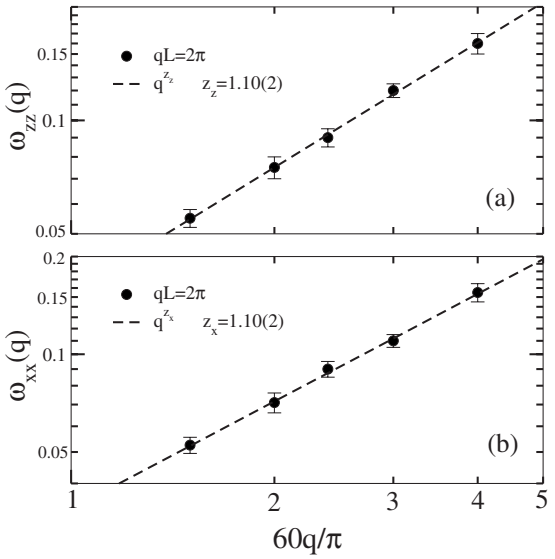

FIG. 14. Log-log plot of the dispersion relation (a) $\omega_{zz}(q)$ and (b) $\omega_{xx}(q)$ as a function of the reduced wave vector at $T=T_t$ in the (100) direction for $qL=2\pi$ and lattices $L=30$, 40, 50, 60, and 80. The dashed line is a linear fit to the data.

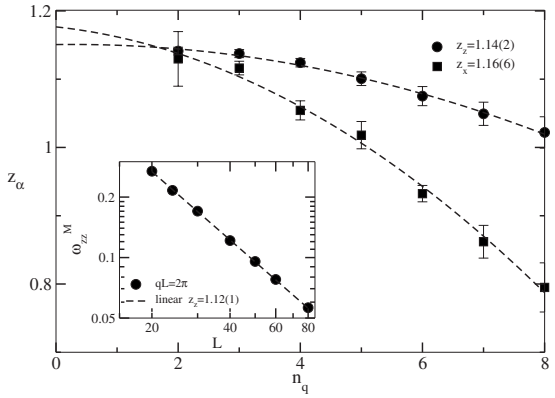

FIG. 15. Critical exponent z_α, $\alpha=z$ and x, as a function of n_q at the tricritical point. The dashed lines are quadratic fits to the data. The inset shows, as an example, the log-log plot of the median frequency ω_{zz}^M as a function of the system sizes for $n_q=1$. The dashed line is a linear fit to the data. Error bars are not larger than the symbol sizes.

smaller, the behavior of the structure factor is still pretty much the same as those corresponding to smaller values of Δ (see Fig. 6), including the presence of two-spin-wave peaks. This can also be understood since $x_3=0.030(1)$ for this case, meaning still a low dilution by the ^{3}He atoms. In fact, Fig. 12 shows the out-of-plane dispersion relation with the spin-dynamic data fitted to Eq. (11) by truncating after the second term with $a_1=3.3187$ and $a_2=-0.1010$. Thus in the ordered phase the general behavior of the dynamics is the same and particularly characteristic of the ^{4}He rich superfluid.

3. Dynamic structure factor at T_t

Here, again, to get the tricritical dynamics in the scaling regime requires much more computational effort. In this case we have considered lattices $L=20$, 24, 30, 40, 50, 60, and 80. In Fig. 13 we show the out-of-plane and in-plane dispersion relations as a function of the wave vector for $q<\pi/2$. For $q\leqslant\pi/15$ the data come from $qL=2\pi$ and $L=30$, 40, 50, 60, and 80, while for $q>\pi/15$ the data are from $n_q>1$ as well as smaller values of L. In this case we can see a deviation from the linear fit, due to the tricritical behavior that sets in, but not so pronounced as in the critical case (see Fig. 8), even for the larger lattices.

Figures 14(a) and 14(b) depict log-log plots of the dispersion relation for small values of q and $L\geqslant 30$. From the linear fit one gets $z_z=1.10(2)$ and $z_x=1.10(3)$. These data clearly show a deviation from a linear behavior which is also evident in Fig. 13; however, the deviation from linearity is not as strong as the corresponding critical behavior of Fig. 8.

We have also used the finite-size scaling of the median frequency to estimate the dynamic critical exponent as conveyed by Eq. (14). The inset in Fig. 15 shows the finite-size scaling behavior of the median frequency ω_{zz}^M as a function of the system size on a log-log scale for $n_q=1$. From these data one gets $z_z=1.12(1)$ which is within the error bar of the previous estimate [see Fig. 14(a)]. One can see that in this estimate all finite lattices follow the scaling regime. The same is not true regarding the median frequency ω_{xx}^M. The presence of a strong central peak in $S^{xx}(q,\omega)$ leads to a median frequency whose data do not follow a well-defined finite-size behavior, mainly for larger lattice sizes (such behavior has been seen in the study of the critical dynamics of the pure model [20]). However, if only the smaller ones are taken we obtain $z_x=1.06(4)$, which is also within the error bar of the result coming from the dispersion relation shown in Fig. 14(b).

We have also done a finite-size scaling by computing the dynamic critical exponent for several values of n_q, as depicted in Fig. 15. The exponents for the out-of-plane fluctuations, z_z, follow a size scaling in which a quadratic fit gives an extrapolated value of $z_z=1.14(2)$ for $n_q=0$. We noted that the in-plane dynamic exponent z_x has a more pronounced size dependence, which also must be due to the presence of the strong central peak in $S^{xx}(q,\omega)$. For this reason the data for z_x come from the smaller lattices. Even so, from the quadratic fit one gets $z_x=1.16(6)$, which agrees with z_z within the error bars.

V. CONCLUDING REMARKS

The static and dynamic properties of the *XY* vector Blume-Emery-Griffiths (*XY*-VBEG) model have been studied by using Monte Carlo spin dynamics simulations. The special case $A=1$, where a tricritical point is present in the phase diagram of the model, has been analyzed in detail. Not only the static critical exponents, but also the dynamic ones, are the same as those of the pure model considered in Ref. [20].

The static tricritical exponents are the corresponding classical ones because the upper critical dimensionality is in this case $d_>=3$. The dynamic tricritical exponents, for the in-plane and out-of-plane fluctuations, are found to be the same, i.e., $z_z=z_x=1.15(4)$. Although Siggia and Nelson [40] examined tricritical "dynamics" in a restricted class of systems, their work does not yield predictions for models of the kind considered here. We are thus unaware of any theoretical predictions with which we could compare our estimates for tricritical dynamic exponents. In contrast, the corresponding dynamic critical exponents are different and, from our simulations we get $z_z=1.39(1)$ and $z_x=1.61(1)$, consistent with the scaling relation $z_z+z_x=3$. As one moves along the second-order line and gets closer to the tricritical point, one expects crossover phenomena not only regarding the static properties, but also for the in-plane and out-of-plane dynamics.

ACKNOWLEDGMENTS

We would like to thank R. T. S. Freire and K. Binder for fruitful discussions regarding the Monte Carlo simulations. This work was funded by CIAM-CNPq Process Grant No. 490101/03-8, NASA Grant No. NNC04GB24, and NSF Grants No. DMR-0341874 and No. DMR-0307082.

[1] P. C. Hohenberg and B. I. Halperin, Rev. Mod. Phys. **49**, 435 (1977).
[2] D. J. Amit and V. Martin-mayor, *Field Theory, the Renormalization Group, and Critical Phenomena*, 3rd ed. (World Scientific, New York, 2005).
[3] G. Parisi, *Statistical Field Theory* (Addison-Wesley, Wokingham, 1988).
[4] R. Folk and G. Moser, J. Phys. A **39**, R207 (2006).
[5] S. Kobe, Braz. J. Phys. **30**, 649 (2000).
[6] R. B. Stinchcombe, in *Phase Transitions and Critical Phenomena*, edited by C. Domb and J. L. Lebowitz (Academic Press, London, 1983), Vol. 7.
[7] D. P. Belanger, Braz. J. Phys. **30**, 682 (2000).
[8] W. P. Wolf, Braz. J. Phys. **30**, 794 (2000).
[9] V. L. Berezinskii, Sov. Phys. JETP **32**, 493 (1971).
[10] J. M. Kosterlitz and D. J. Thouless, J. Phys. C **6**, 1181 (1973).
[11] L. E. Svistov, A. I. Smirnov, L. A. Prozorova, O. A. Petrenko, A. Micheler, N. Buttgen, A. Y. Shapiro, and L. N. Demianets, Phys. Rev. B **74**, 024412 (2006).
[12] D. G. Wiesler, H. Zabel, and S. M. Shapiro, Z. Phys. B: Condens. Matter **93**, 277 (1994).
[13] M. T. Hutchings, P. Day, E. Janke, and R. Pynn, J. Magn. Magn. Mater. **54**, 673 (1986).
[14] K. Hirakawa and H. Yoshizawa, J. Phys. Soc. Jpn. **47**, 368 (1979).
[15] S. A. Liu, Q. Wang, H. Li, and T. L. Chen, Commun. Theor. Phys. **32**, 339 (1999).
[16] S. W. Pierson, Phys. Rev. B **51**, 6663 (1995).
[17] M.-S. Choi and S.-I. Lee, Phys. Rev. B **51**, 6680 (1995).
[18] M. Franz and A. P. Iyengar, Phys. Rev. Lett. **96**, 047007 (2006).
[19] T. Matsubara and H. Matsuda, Prog. Theor. Phys. **16**, 569 (1956).
[20] M. Krech and D. P. Landau, Phys. Rev. B **60**, 3375 (1999).
[21] K. Nho and E. Manousakis, Phys. Rev. B **64**, 144513 (2001).
[22] E. H. Graf, D. M. Lee, and J. D. Reppy, Phys. Rev. Lett. **19**, 417 (1967).
[23] H. A. Kierstead, J. Low Temp. Phys. **35**, 25 (1979).
[24] M. Blume, V. J. Emery, and R. B. Griffiths, Phys. Rev. A **4**, 1071 (1971).
[25] A. N. Berker and D. R. Nelson, Phys. Rev. B **19**, 2488 (1979).
[26] J. L. Cardy and D. J. Scalapino, Phys. Rev. B **19**, 1428 (1979).
[27] A. Maciolek, M. Krech, and S. Dietrich, Phys. Rev. E **69**, 036117 (2004).
[28] R. T. S. Freire, S. J. Mitchell, J. A. Plascak, and D. P. Landau, Phys. Rev. E **72**, 056117 (2005).
[29] S.-H. Tsai and D. P. Landau, Phys. Rev. B **67**, 104411 (2003).
[30] J. A. Plascak, A. M. Ferrenberg, and D. P. Landau, Phys. Rev. E **65**, 066702 (2002).
[31] W. H. Press, B. P. Flannery, S. A. Teukolsky, and W. T. Vetterling, *Numerical Recipes in Fortran 77*, 2nd ed. (Cambridge University Press, New York, 1992), Vol. 1.
[32] D. P. Landau and M. Krech, J. Phys.: Condens. Matter **11**, R179 (1999).
[33] S.-H. Tsai, M. Krech, and D. P. Landau, Braz. J. Phys. **34**, 384 (2004).
[34] S.-H. Tsai, H. K. Lee, and D. P. Landau, Am. J. Phys. **73**, 615 (2005).
[35] M. Krech, A. Bunker, and D. P. Landau, Comput. Phys. Commun. **111**, 1 (1998).
[36] J. Frank, W. Huang, and B. Leimkuhler, J. Comput. Phys. **133**, 160 (1997).
[37] M. Campostrini, M. Hasenbusch, A. Pelissetto, and E. Vicari, Phys. Rev. B **74**, 144506 (2006).
[38] M. Hasenbusch, J. Stat. Mech.: Theory Exp. P08019 (2006).
[39] S. Thoma, E. Frey, and F. Schwabl, Phys. Rev. B **43**, 5831 (1991).
[40] E. D. Siggia and D. R. Nelson, Phys. Rev. B **15**, 1427 (1977).